

# Adaptive Partial Differential Equation Observer for Battery State-of-Charge/State-of-Health Estimation Via an Electrochemical Model

**Scott J. Moura**

UC President's Postdoctoral Fellow  
Mechanical and Aerospace Engineering,  
University of California, San Diego,  
San Diego, CA 92093  
e-mail: smoura@ucsd.edu

**Nalin A. Chaturvedi**

Senior Research Engineer  
Research and Technology Center,  
Robert Bosch LLC,  
Palo Alto, CA 94304  
e-mail: nalin.chaturvedi@us.bosch.com

**Miroslav Krstić**

Professor  
Mechanical and Aerospace Engineering,  
University of California, San Diego,  
San Diego, CA 92093  
e-mail: krstic@ucsd.edu

*This paper develops an adaptive partial differential equation (PDE) observer for battery state-of-charge (SOC) and state-of-health (SOH) estimation. Real-time state and parameter information enables operation near physical limits without compromising durability, thereby unlocking the full potential of battery energy storage. SOC/SOH estimation is technically challenging because battery dynamics are governed by electrochemical principles, mathematically modeled by PDEs. We cast this problem as a simultaneous state (SOC) and parameter (SOH) estimation design for a linear PDE with a nonlinear output mapping. Several new theoretical ideas are developed, integrated together, and tested. These include a backstepping PDE state estimator, a Padé-based parameter identifier, nonlinear parameter sensitivity analysis, and adaptive inversion of nonlinear output functions. The key novelty of this design is a combined SOC/SOH battery estimation algorithm that identifies physical system variables, from measurements of voltage and current only. [DOI: 10.1115/1.4024801]*

## 1 Introduction

This paper develops an adaptive PDE observer for combined SOC and SOH estimation in batteries, using an electrochemical model.

Accurate battery SOC estimation algorithms are currently of extreme importance due to their applications in electrified transportation and energy storage systems for renewable sources. The relevancy of this topic is further underscored by the 27.2 billion USD federal government investment in energy efficiency and renewable energy research, including advanced batteries, under the American Recovery and Reinvestment Act of 2009. To guarantee safety, durability, and performance, battery management systems within these advanced transportation and energy infrastructures must have accurate knowledge of internal battery energy levels [1]. Such knowledge enables them to efficiently route energy while satisfying power demands and device-level operating constraints [2].

Monitoring battery SOC and SOH is particularly challenging for several technical reasons. First, directly measuring Li concentration or physical examination of cell components is impractical outside specialized laboratory environments [3,4]. Second, the dynamics are governed by partial differential algebraic equations derived from electrochemical principles [5]. The only measurable quantities (voltage and current) are related to the states through boundary values. Finally, the model's parameters vary widely with electrode chemistry, electrolyte, packaging, and time. In this paper, we directly address these technical challenges. Namely, we design an adaptive observer using a reduced-form PDE model based upon electrochemical principles. As such, the algorithm estimates physical variables directly related to SOC and SOH, a first to the authors' knowledge.

Over the past decade research on battery SOC/SOH estimation has experienced considerable growth. One may divide this research by the battery models each algorithm employs.

The first category considers estimators based upon equivalent circuit models (ECMs). These models use circuit elements to mimic the phenomenological behavior of batteries. For example, the work by Plett [6] applies an extended Kalman filter to simultaneously identify the states and parameters of an ECM. Verbrugge and his co-workers used ECMs with combined coulomb-counting and voltage inversion techniques in Ref. [7] and adaptive parameter identification algorithms in Ref. [8]. More recently, a linear parameter varying approach was designed in Ref. [9]. The key advantage of ECMs is their simplicity. However, they often require extensive parameterization for accurate predictions. This often produces models with nonphysical parameters, whose complexity becomes comparable to electrochemical models.

The second category considers electrochemical models, which account for the diffusion, intercalation, and electrochemical kinetics. Although these models can accurately predict internal state variables, their mathematical structure is generally too complex for controller/observer design. Therefore, these approaches combine model reduction and estimation techniques. Some of the first studies within this category use a "single particle model" (SPM) of electrochemical battery dynamics in combination with an extended Kalman filter [10,11]. Another approach is to employ residue grouping for model reduction and linear Kalman filters for observers [12]. The authors of Ref. [13] apply simplifications to the electrolyte and solid phase concentration dynamics to perform SOC estimation. To date, however, simultaneous SOC and SOH estimation using electrochemical models remains an open question.

In this paper, we extend the aforementioned research by designing an electrochemical model based adaptive observer for simultaneous SOC/SOH estimation. Several novel theoretical ideas are developed, integrated, and tested. These include a PDE backstepping state estimator, Padé-based PDE parameter

Contributed by the Dynamic Systems Division of ASME for publication in the JOURNAL OF DYNAMIC SYSTEMS, MEASUREMENT, AND CONTROL. Manuscript received July 18, 2012; final manuscript received June 8, 2013; published online October 15, 2013. Assoc. Editor: Yang Shi.

identifier, nonlinear identifiability analysis of the output equation, and adaptive output function inversion. This paper extends our previous work [14–16] by including estimator validation results against a high-fidelity battery simulator. The final result is an adaptive observer for simultaneous SOC/SOH estimation which identifies physical battery system variables, from current and voltage measurements only.

The paper is organized as follows: Sec. 2 describes the single particle model. Sections 3–6 describe the subsystems of the adaptive observer, including the state estimator, PDE parameter identifier, output function parameter identifier, and adaptive output function inversion. Section 7 presents simulation results to demonstrate the observer’s performance. Section 8 provides guidelines for selecting gains. Finally, Sec. 9 summarizes the key contributions.

## 2 Electrochemical Cell Model and Analysis

The SPM was first applied to lithium battery systems in Ref. [17] and is the model we utilize in this paper. The key idea is that the solid phase of each electrode can be idealized as a single spherical particle. This model results if one assumes the electrolyte Li concentration is constant in space and time [1]. This assumption works well for small currents or electrolytes with large electronic conductivities. However, it induces errors at large C-rates [1]. Moreover, we assume constant temperature. Figure 1 provides a schematic of the SPM concept. Mathematically, the model consists of two diffusion PDEs governing each electrode’s concentration dynamics, where input current enters as a Neumann boundary condition. Output voltage is given by a nonlinear function of the state values at the boundary and the input current.

Although this model captures less dynamic behavior than other electrochemical-based estimation models [17], its mathematical structure is amenable to adaptive observer design.

**2.1 Single Particle Model.** Diffusion in each electrode is governed by Fick’s law in spherical coordinates

$$\frac{\partial c_s^-}{\partial t}(r, t) = D_s^- \left[ \frac{2}{r} \frac{\partial c_s^-}{\partial r}(r, t) + \frac{\partial^2 c_s^-}{\partial r^2}(r, t) \right] \quad (1)$$

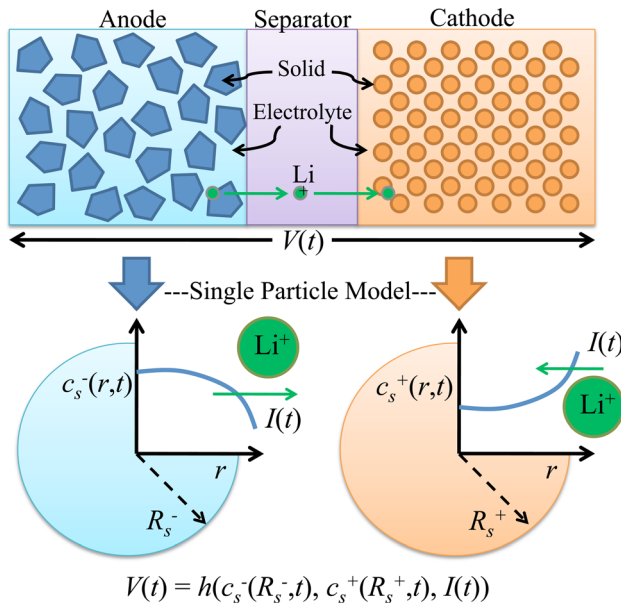


**Fig. 1** Each electrode is idealized as a single porous spherical particle. This model results from assuming the electrolyte concentration is constant in space and time.

$$\frac{\partial c_s^+}{\partial t}(r, t) = D_s^+ \left[ \frac{2}{r} \frac{\partial c_s^+}{\partial r}(r, t) + \frac{\partial^2 c_s^+}{\partial r^2}(r, t) \right] \quad (2)$$

with Neumann boundary conditions

$$\frac{\partial c_s^-}{\partial r}(0, t) = 0, \quad \frac{\partial c_s^-}{\partial r}(R_s^-, t) = \frac{I(t)}{D_s^- F a^- AL^-} \quad (3)$$

$$\frac{\partial c_s^+}{\partial r}(0, t) = 0, \quad \frac{\partial c_s^+}{\partial r}(R_s^+, t) = -\frac{I(t)}{D_s^+ F a^+ AL^+} \quad (4)$$

The Neumann boundary conditions at  $r = R_s^+$  and  $r = R_s^-$  signify that the flux entering the electrode is proportional to the input current  $I(t)$ . The Neumann boundary conditions at  $r = 0$  are required for well-posedness. Note that the states for the two PDEs are dynamically uncoupled, although they have proportional boundary inputs.

The measured terminal voltage output is governed by a combination of electric overpotential, electrode thermodynamics, and Butler-Volmer kinetics. The end result is

$$V(t) = \frac{RT}{\alpha F} \sinh^{-1} \left( \frac{I(t)}{2a^+ AL^+ i_0^+(c_{ss}^+(t))} \right) - \frac{RT}{\alpha F} \sinh^{-1} \left( \frac{I(t)}{2a^- AL^- i_0^-(c_{ss}^-(t))} \right) + U^+(c_{ss}^+(t)) - U^-(c_{ss}^-(t)) + R_f I(t) \quad (5)$$

where the exchange current density  $i_0^j$  and solid-electrolyte surface concentration  $c_{ss}^j$  are, respectively

$$i_0^j(c_{ss}^j) = k^j \sqrt{c_s^0 c_{ss}^j(t) (c_{s, \max}^j - c_{ss}^j(t))} \quad (6)$$

$$c_{ss}^j(t) = c_s^j(R_s^j, t), \quad j \in \{+, -\} \quad (7)$$

The functions  $U^+(\cdot)$  and  $U^-(\cdot)$  in Eq. (5) are the equilibrium potentials of each electrode material, given the surface concentration. Mathematically, these are strictly monotonically decreasing functions of their input. This fact implies that the inverse of its derivative is always finite, a property which we require in Sec. 6. Further details on the electrochemical principles used to derive these equations can be found in Refs. [1,5].

This model contains the property that the total number of lithium ions is conserved [13]. Mathematically,  $(d/dt)(n_{Li}) = 0$ , where

$$n_{Li} = \frac{\varepsilon_s^+ L^+ A}{\frac{4}{3} \pi (R_s^+)^3} \int_0^{R_s^+} 4\pi r^2 c_s^+(r, t) dr + \frac{\varepsilon_s^- L^- A}{\frac{4}{3} \pi (R_s^-)^3} \int_0^{R_s^-} 4\pi r^2 c_s^-(r, t) dr \quad (8)$$

This property will become important, as it relates the total concentration of lithium in the cathode and anode. We leverage this fact to perform model reduction in the state estimation problem.

**2.2 Model Comparison.** The SPM approximation increases in accuracy as C-rate decreases and/or as electrolyte conductivity increases. Here, we demonstrate how the SPM’s accuracy degrades as C-rate increases, compared to a full order electrochemical model.

A simulator has been created for the so-called Doyle-Fuller-Newman (DFN) model described in Ref. [1]. This model retains the electrolyte dynamics and spatial dynamics across the width of the electrode. Figure 2 presents a freeze-frame of the solid and electrolyte Li concentrations after 50 s of 5 C discharge. This high discharge rate induces notable concentration gradients in the electrolyte, which the SPM will not predict. The parameters are

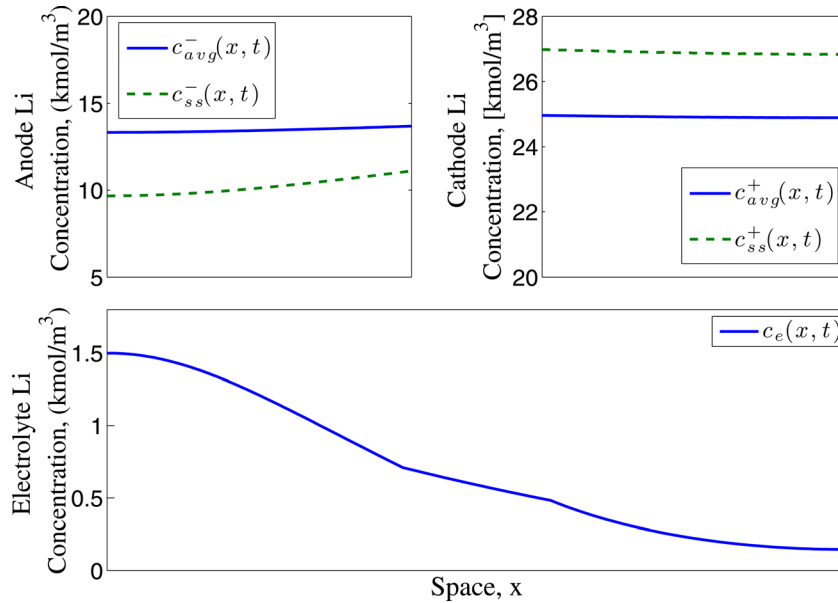


**Fig. 2** DFN predictions of the solid and electrolyte concentrations as functions of space. The DFN model retains electrolyte and spatial dynamics. State values are depicted after 50 s of 5C discharge. Symbol  $c_{avg}$  is the solid concentration averaged over a spherical particle and  $c_{ss}$  is the surface concentration. Note the non-negligible concentration gradients in the electrolyte.

identical to those used in the publicly available DUALFOIL model, developed by Newman and his collaborators [18]. This DFN model also serves as the generator of experimental data to evaluate the adaptive observer's performance.

The voltage response to several constant discharge rates is presented in Fig. 3. For complete discharge cycles, the maximum sustainable C-rate for this model parameterization is 1.25C. Higher C-rates will completely deplete the electrolyte lithium in the cathode. All simulations are initialized at 4.06 V and terminated when terminal voltage reaches 2.0 V. The voltage error increases as C-rate increases. At higher C-rates, the electrolyte concentration gradients become significant with respect to their impact on terminal voltage. At low C-rates, the concentration gradients are negligible and therefore a uniform approximation is a reasonable assumption. It is important to note the predicted charge capacity is identical between both models. This property is critical for applications where charge capacity is important, e.g., electric vehicles. In spite of the SPM's errors at high C-rates, adaptive

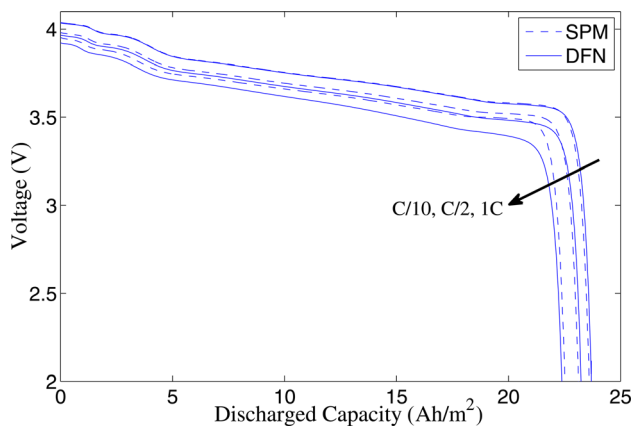


**Fig. 3** Voltage response for several discharge rates, for the SPM and DFN model. The SPM exhibits increasing error as C-rate increases, but identical discharge capacities.

observer design for this model is significantly easier than the DFN model, although highly nontrivial.

In the following sections, we describe each subsystem of the adaptive observer. A block diagram of the composed system is provided in Fig. 4.

### 3 State Estimation

**3.1 Observability and Model Reduction.** For the purpose of observer design we reduce the SPM by approximating the cathode diffusion dynamics (2) by its equilibrium. This step is mathematically motivated by the fact that the SPM states are weakly observable from voltage measurements, as has been previously noted in the literature [11]. It turns out that approximating the cathode dynamics as instantaneous produces a reduced system whose states are locally observable in the linear sense. Moreover, physical motivation exists for this reduction when diffusion dynamics are significantly faster in the cathode than the anode, a common characteristic of certain anode/cathode combinations. We discuss these points in succession.

Lack of observability can be shown using a number of techniques. For example, one may (i) approximate the PDEs by ODEs using the finite difference method, producing a tri-diagonal matrix  $A$ , (ii) linearize the output equation about the states, producing a matrix  $C$ , (iii) and compute the rank of the observability matrix for the pair  $(A, C)$  [19].

The reduced SPM has a PDE given by Eq. (1), boundary conditions given by Eq. (3), and output equation

$$\begin{aligned}
 V(t) = & \frac{RT}{\alpha^+ F} \sinh^{-1} \left( \frac{I(t)}{2a^+ AL^+ i_0^+ (\alpha c_{ss}^-(t) + \beta)} \right) \\
 & - \frac{RT}{\alpha^- F} \sinh^{-1} \left( \frac{I(t)}{2a^- AL^- i_0^- (c_{ss}^-(t))} \right) \\
 & + U^+ (\alpha c_{ss}^-(t) + \beta) - U^- (c_{ss}^-(t)) - R_f I(t) \quad (9)
 \end{aligned}$$

Note that  $c_{ss}^+(t)$  has been replaced by  $\alpha c_{ss}^-(t) + \beta$ . This is the critical detail of the reduced SPM. The equilibrium of the cathode

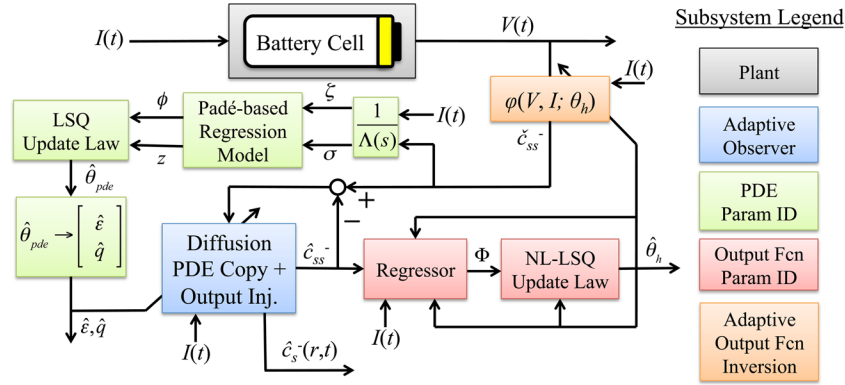


**Fig. 4** Block diagram of the adaptive observer. It is composed of the backstepping state estimator (blue), PDE parameter identifier (green), output function parameter identifier (red), and adaptive output function inversion (orange). The observer furnishes estimates of SOC (i.e.,  $\hat{c}_s^-(r, t)$ ) and SOH (i.e.,  $\hat{e}, \hat{q}, \hat{\theta}_n$ ) given measurements of  $I(t)$  and  $V(t)$ , only.

states (i.e.,  $c_s^+(r, t) = c_{ss}^+(t)$ ) can be computed from the conservation of Li property in Eq. (8) to produce the relationship<sup>1</sup>

$$c_{ss}^+(t) = \frac{1}{\varepsilon_s^+ L + A} [n_{Li} - \varepsilon_s^- L^- A c_{ss}^-(t)] \quad (10)$$

where  $\alpha = -(\varepsilon_s^- L^- / \varepsilon_s^+ L^+)$  and  $\beta = (n_{Li} / \varepsilon_s^+ L^+ A)$ .

One can show this system is locally observable (i.e., in the linear sense) by using the same finite difference and linearization approach described above. Ultimately, we guarantee observability for this reduced SPM by designing the observer gains such that the estimation error dynamics mimic an exponentially stable target system. This is the core concept behind backstepping observer design [20].

Physical motivation sometimes exists for approximating the cathode diffusion dynamics as instantaneous. Significant research efforts on manufacturing and material science techniques for cathode materials have enabled researchers to attain nanoscale particle sizes and faster diffusion rates [21]. The result is characteristic diffusion times (mathematically  $R_s^2 / D_s$ ) which are often orders of magnitude less in the cathode than the anode. Parallel studies have been performed on the anode side (see e.g., Ref. [22]), however they are less prevalent. Hence, approximating cathode diffusion by its equilibrium is a reasonable approximation for certain cathode/anode combinations. This insight was also observed through a previous parameter identification study on commercially available LiFePO<sub>4</sub> cells with doped nanoscale cathode materials [23]. For other cells, the required diffusive time scale separation property may not exist.

**3.2 Normalization and State Transformation.** Next, we perform normalization and state transformation to simplify the mathematical structure of the observer. First scale the radial  $r$  and time  $t$  coordinates as follows:

$$\bar{r} = \frac{r}{R_s^-}, \quad \bar{t} = \frac{D_s^-}{(R_s^-)^2} t \quad (11)$$

Henceforth, we will drop the bars over the space and time coordinates to simplify notation. Next, we perform a state transformation

<sup>1</sup>To be technically correct, the cathode concentration should depend on the anode concentration summed over the spherical volume:  $c_{ss}^+(t) = (1 / \varepsilon_s^+ L^+ A) [n_{Li} - (3 \varepsilon_s^- L^- A / 4 \pi R_s^3) \int_0^{R_s} 4 \pi r^2 c_s^-(r, t) dr]$ . However, this results in a nonlinear output equation which depends on the in-domain states, as well as the boundary state. This would create additional complexity to the backstepping approach we employ in this paper.

to eliminate the first spatial derivative in the spherical diffusion Eq. (1). Namely, let

$$c(r, t) = r c_s^-(r, t) \quad (12)$$

This normalization and state transformation produces the following PDE with Dirichlet and Robin boundary conditions

$$\frac{\partial c}{\partial t}(r, t) = \varepsilon \frac{\partial^2 c}{\partial r^2}(r, t) \quad (13)$$

$$c(0, t) = 0 \quad (14)$$

$$\frac{\partial c}{\partial r}(1, t) - c(1, t) = -q\rho I(t) \quad (15)$$

and nonlinear output map given by Eq. (9), where  $c_{ss}^+ = \alpha c(1, t) + \beta$  (see Eq. (10)), and  $c_{ss}^- = c(1, t)$ . The parameter  $\rho = R_s^- / (D_s^- F a^- A L^-)$  groups together known parameters. The parameters  $\varepsilon$  and  $q$  are nominally equal to one. Respectively, they represent uncertainty in the diffusion and boundary input coefficients, which we identify in Sec. 4.

**3.3 Backstepping PDE State Estimator.** The SPM comprises linear dynamics and a nonlinear output function. In general an output injection-based estimator would be nonlinear for this class of systems. However, we design a linear estimator in this paper by injecting the boundary state error. This idea requires us to calculate the boundary state from the measured voltage, demonstrated visually by the block diagram in Fig. 4. In Ref. [14], we show the output function (9) is invertible with respect to the boundary state  $c_{ss}^-$ , uniformly in the input current  $I(t)$ .

The state estimator structure consists of a copy of the plant (13)–(15) plus boundary state error injection, as follows:

$$\frac{\partial \hat{c}}{\partial t}(r, t) = \varepsilon \frac{\partial^2 \hat{c}}{\partial r^2}(r, t) + p_1(r) \tilde{c}(1, t) \quad (16)$$

$$\hat{c}(0, t) = 0 \quad (17)$$

$$\frac{\partial \hat{c}}{\partial r}(1, t) - \hat{c}(1, t) = -q\rho I(t) + p_{10} \tilde{c}(1, t) \quad (18)$$

where the boundary state error is given by

$$\tilde{c}(1, t) = \varphi(V(t), I(t)) - \hat{c}(1, t) \quad (19)$$

The backstepping approach [20] is applied to design the output injection gains  $p_1(r)$  and  $p_{10}$ . First, denote the observer error

as  $\tilde{c}(r, t) = c(r, t) - \hat{c}(r, t)$ . Subtracting Eqs. (16)–(18) from Eqs. (13) to (15) produces the estimation error dynamics

$$\frac{\partial \tilde{c}}{\partial t}(r, t) = \varepsilon \frac{\partial^2 \tilde{c}}{\partial r^2}(r, t) - p_1(r) \tilde{c}(1, t) \quad (20)$$

$$\tilde{c}(0, t) = 0 \quad (21)$$

$$\frac{\partial \tilde{c}}{\partial r}(1, t) - \tilde{c}(1, t) = -p_{10} \tilde{c}(1, t) \quad (22)$$

The backstepping approach seeks to find the upper-triangular transformation

$$\tilde{c}(r, t) = \tilde{w}(r, t) - \int_r^1 p(r, s) \tilde{w}(s) ds \quad (23)$$

which satisfies the exponentially stable target system

$$\frac{\partial \tilde{w}}{\partial t}(r, t) = \varepsilon \frac{\partial^2 \tilde{w}}{\partial r^2}(r, t) + \lambda \tilde{w}(r, t) \quad (24)$$

$$\tilde{w}(0, t) = 0 \quad (25)$$

$$\frac{\partial \tilde{w}}{\partial r}(1, t) = -\frac{1}{2} \tilde{w}(1, t) \quad (26)$$

where  $\lambda < \varepsilon/4$ . The symbol  $\lambda$  is a design parameter that enables us to adjust the pole placement of the observer. The coefficient  $-1/2$  in Eq. (26) ensures the target system is exponentially stable, as can be seen by the derivation below.

One can show that Eqs. (24)–(26) is exponentially stable in the spatial  $L_2$  norm by considering the Lyapunov function

$$W(t) = \frac{1}{2} \int_0^1 \tilde{w}^2(r, t) dr \quad (27)$$

Taking the total time derivative and applying integration by parts yields

$$\dot{W}(t) = -\frac{\varepsilon}{2} \tilde{w}^2(1) - \varepsilon \int_0^1 \tilde{w}_r^2 dr + \lambda \int_0^1 \tilde{w}^2 dr \quad (28)$$

Recalling the Poincaré inequality

$$-\varepsilon \int_0^1 \tilde{w}_r^2 dr \leq \frac{\varepsilon}{2} \tilde{w}^2(1) - \frac{\varepsilon}{4} \int_0^1 \tilde{w}^2 dr \quad (29)$$

produces

$$\dot{W}(t) \leq -\left(\frac{\varepsilon}{4} - \lambda\right) \int_0^1 \tilde{w}^2 dr = -\left(\frac{\varepsilon}{2} - 2\lambda\right) W(t) \quad (30)$$

which by the comparison principle [24] implies  $W(t) \leq W(0) \exp[-(\varepsilon/2 - 2\lambda)t]$  or  $\|\tilde{w}(t)\| \leq \|\tilde{w}(0)\| \exp[-(\varepsilon/4 - \lambda)t]$ . Hence, the target system is exponentially stable for  $\lambda < \varepsilon/4$ .

*Remark 1.* Using separation of variables, one may show the eigenvalues for the target system, (and hence the error system) are  $\lambda - \varepsilon y^2$ , where  $y$  is given by the solutions of  $y + \frac{1}{2} \tan(y) = 0$ . Consequently, the eigenvalues have zero imaginary parts. As  $\lambda \rightarrow -\infty$ , the eigenvalue spectrum translates toward  $-\infty$ .

Following the procedure outlined in Ref. [20], we find that the kernel  $p(r, s)$  in Eq. (23) must satisfy the following conditions:

$$p_{rr}(r, s) - p_{ss}(r, s) = \frac{\lambda}{\varepsilon} p(r, s) \quad (31)$$

$$p(0, s) = 0 \quad (32)$$

$$p(r, r) = \frac{\lambda}{2\varepsilon} r \quad (33)$$

defined on the domain  $\mathcal{D} = \{(r, s) | 0 \leq r \leq s \leq 1\}$ . The output injection gains are

$$p_1(r) = -p_s(r, 1) - \frac{1}{2} p(r, 1) \quad (34)$$

$$p_{10} = \frac{3 - \lambda/\varepsilon}{2} \quad (35)$$

These conditions compose a Klein-Gordon PDE, which coincidentally has an analytic solution given by

$$p(r, s) = \frac{\lambda}{\varepsilon} r \frac{I_1(\sqrt{\lambda/\varepsilon}(r^2 - s^2))}{\sqrt{\lambda/\varepsilon}(r^2 - s^2)} \quad (36)$$

Solution Eq. (36) can be derived by converting the PDE into an equivalent integral equation and applying the method of successive approximations [20]. Ultimately, this closed form solution provides the following output injection gains:

$$p_1(r) = \frac{-\lambda r}{2\varepsilon z} \left[ I_1(z) - \frac{2\lambda}{\varepsilon z} I_2(z) \right] \quad (37)$$

$$\text{where } z = \sqrt{\frac{\lambda}{\varepsilon}}(r^2 - 1) \quad (38)$$

$$p_{10} = \frac{1}{2} \left( 3 - \frac{\lambda}{\varepsilon} \right) \quad (39)$$

and  $I_1(z)$  and  $I_2(z)$  are, respectively, the first and second order modified Bessel functions of the first kind.

To complete the design, we need to establish that stability of the target system Eqs. (24)–(26) implies stability of the error system (20)–(22). That is, we must show the transformation (23) is invertible. Toward this end, write the inverse transformation as

$$\tilde{w}(r, t) = \tilde{c}(r, t) + \int_r^1 l(r, s) \tilde{c}(s) ds \quad (40)$$

Following the same approach used to derive the direct transformation kernel (36), we find that the inverse transformation kernel has the analytic solution

$$l(r, s) = \frac{\lambda}{\varepsilon} r \frac{J_1(\sqrt{\lambda/\varepsilon}(r^2 - s^2))}{\sqrt{\lambda/\varepsilon}(r^2 - s^2)} \quad (41)$$

where  $J_1$  is the first order Bessel function of the first kind. We now state the main result for the backstepping state estimator.

**THEOREM 1.** Consider the plant model (13)–(15) with observer (16)–(19) and estimation gains (37)–(39). Then  $\exists \lambda < \varepsilon/4$  such that the origin of the error system  $\tilde{c} = 0$  is exponentially stable in the  $L^2(0, 1)$  norm.

*Remark 2.* Note that the estimator is linear in the state because we use the boundary state for error injection. The plant boundary state is computed by inverting the nonlinear output mapping with respect to the boundary state, given a current input (i.e.,  $\varphi(V(t), I(t))$ ). The output function inversion is discussed in detail in Sec. 6.

*Remark 3.* Note the parameters  $\varepsilon$  in Eqs. (16), (37)–(39) and  $q$  in Eq. (18). In the subsequent section, we design an identifier for these parameters. We form an adaptive observer by replacing these parameters with their estimates, via the certainty equivalence principle [25].

#### 4 PDE Parameter Identification

Next, we design an identification algorithm for the diffusion and boundary input coefficients in Eqs. (13) and (15), respectively. Identification of the diffusion coefficient  $\varepsilon$  from boundary

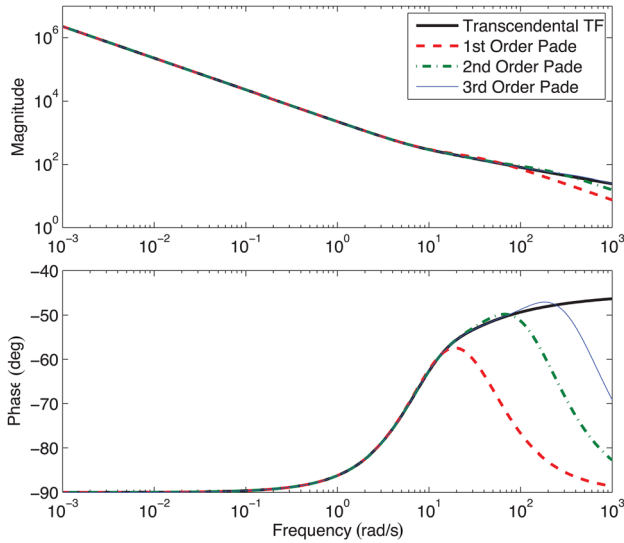


**Fig. 5 Bode plots of the transcendental transfer function (42) and Padé approximants in Table 1**

measurements is a significant fundamental challenge [26], for the following reason. In finite-dimensional state-space systems, we typically write the system in observable canonical form. This structure enables one to uniquely identify state-space parameters from input–output data. In our problem, we require a parametric model where the diffusion coefficient multiplies measured data only. Otherwise, we have a nonlinear problem, since unknown states are multiplied by unknown parameters. There is no clear way to do this for PDEs. This motivates our new contribution: utilizing a reduced-order model (Padé approximation) for the parameter identification.

**4.1 Padé Approximates.** The PDE model Eqs. (13)–(15) can be written in the frequency domain as a transcendental transfer function

$$G(s) = \frac{c_{ss}(s)}{I(s)} = \frac{-q\rho \sinh(\sqrt{s/\varepsilon})}{(\sqrt{s/\varepsilon}) \cosh(\sqrt{s/\varepsilon}) - \sinh(\sqrt{s/\varepsilon})} \quad (42)$$

We now apply Padé approximations of the transcendental transfer function (42). Padé approximants represent a function by a ratio of two power series. The defining characteristic of a Padé approximant is that its Taylor series matches the Taylor series of the function it is approximating. Another useful property of Padé approximants is that they naturally contain poles and zeros. The Padé expansion takes the following form:

$$G(s) = \lim_{N \rightarrow \infty} \frac{\sum_{k=0}^N b_k s^k}{1 + \sum_{k=1}^N a_k s^k} \quad (43)$$

Figure 5 provides bode plots of  $G(s)$  and several Padé approximants. Their analytical expressions are supplied in Table 1. The Padé approximants capture low frequency dynamics well. Accuracy at high frequency increases as the Padé order increases. We low-pass filter the input–output signals such that data are retained where the Padé approximation is sufficiently accurate.

Our immediate goal is to design a parameter identification scheme for the Padé approximation of the original PDE model.

**Table 1 Padé approximants of the PDE model (13)–(15)**

Order, $k$	$P_k(s)$
1	$\frac{-q\rho \left( \frac{2}{7}s + 3\varepsilon \right)}{s \left( \frac{1}{35\varepsilon}s + 1 \right)}$
2	$\frac{-q\rho \left( \frac{1}{165\varepsilon}s^2 + \frac{4}{11}s + 3\varepsilon \right)}{s \left( \frac{1}{3465\varepsilon^2}s^2 + \frac{3}{55\varepsilon}s + 1 \right)}$
3	$\frac{-q\rho \left( \frac{4}{75075\varepsilon^2}s^3 + \frac{2}{195\varepsilon}s^2 + \frac{2}{5}s + 3\varepsilon \right)}{s \left( \frac{1}{675675\varepsilon^3}s^3 + \frac{2}{2275\varepsilon^2}s^2 + \frac{1}{15\varepsilon}s + 1 \right)}$

**4.2 Least Squares Identification.** We utilize the first order Padé approximant as the nominal model. Namely

$$\frac{C_{ss}(s)}{I(s)} \approx P_1(s) = \frac{-3q\rho\varepsilon - \frac{2}{7}q\rho s}{s + \frac{1}{35\varepsilon}s^2} \quad (44)$$

Assuming zero initial conditions and applying the inverse Laplace transform produces the following linearly parameterized model:

$$\frac{1}{35} \ddot{c}_{ss}(t) = -\varepsilon \dot{c}_{ss}(t) - 3\rho q \varepsilon^2 I(t) - \frac{2}{7} \rho q \varepsilon I(t) \quad (45)$$

Since the parametric model contains time derivatives of measured signals, we employ filters [25] to avoid differentiation as follows:

$$\dot{\sigma}_1 = \sigma_2 \quad (46)$$

$$\dot{\sigma}_2 = -\lambda_0 \sigma_1 - \lambda_1 \sigma_2 + c_{ss} \quad (47)$$

$$\dot{\zeta}_1 = \zeta_2 \quad (48)$$

$$\dot{\zeta}_2 = -\lambda_0 \zeta_1 - \lambda_1 \zeta_2 + I \quad (49)$$

where the polynomial  $\Lambda(s) = s^2 + \lambda_1 s + \lambda_0$  is chosen Hurwitz. One can analytically show that selecting the roots of  $\Lambda(s)$  results in a trade-off between convergence rate (via level of persistence of excitation) and parameter bias (error induced by Padé approximation). Consequently, the parametric model is given by

$$\frac{1}{35} (-\lambda_0 \sigma_1 - \lambda_1 \sigma_2 + c_{ss}) = -3\rho q \varepsilon^2 \zeta_1 - \frac{2}{7} \rho q \varepsilon \zeta_2 - \varepsilon \sigma_2 \quad (50)$$

Let us denote the vector of unknown parameters by

$$\theta_{pde} = [q\varepsilon^2 \quad q\varepsilon \quad \varepsilon]^T \quad (51)$$

Then, the parametric model can be expressed in matrix form as  $z_{pde} = \theta_{pde}^T \phi$ , where

$$z_{pde} = \frac{1}{35} (-\lambda_0 \sigma_1 - \lambda_1 \sigma_2 + c_{ss}) \quad (52)$$

$$\phi = \left[ -3\rho \zeta_1 \quad -\frac{2}{7} \rho \zeta_2 \quad -\sigma_2 \right]^T \quad (53)$$

Given this linearly parameterized model, we choose a least-squares update law of the form [25]

$$\dot{\hat{\theta}}_{pde} = P_{pde} \frac{z_{pde} - \hat{\theta}_{pde}^T \phi}{m_{pde}^2} \phi \quad (54)$$

$$\dot{P}_{pde} = -P_{pde} \frac{\phi \phi^T}{m_{pde}^2} P_{pde}, \quad P_{pde}(0) = P_{pde0} = P_{pde0}^T > 0 \quad (55)$$

$$m_{pde}^2 = 1 + \gamma_{pde} \phi^T \phi, \quad \gamma_{pde} > 0 \quad (56)$$

**4.2.1 Managing Overparameterization With the Moore-Penrose Pseudoinverse.** An important implementation issue with the proposed Padé approximation approach is overparameterization. That is, the physical parameters must be uniquely determined from the parameter vector  $\hat{\theta}_{pde}$

$$\hat{\theta}_{pde} = \begin{bmatrix} \widehat{q\hat{\varepsilon}^2} \\ \widehat{q\hat{\varepsilon}} \\ \widehat{\hat{\varepsilon}} \end{bmatrix} \rightarrow \begin{bmatrix} \hat{\varepsilon} \\ \hat{q} \end{bmatrix} = \hat{\theta}_{eq} \quad (57)$$

Coincidentally, the particular nonlinear form (products and powers) of the elements in vector  $\hat{\theta}_{pde}$  allows us to write a set of *linear equations* using a logarithmic nonlinear transformation and properties of the logarithm function

$$\begin{bmatrix} 2 & 1 \\ 1 & 1 \\ 1 & 0 \end{bmatrix} \begin{bmatrix} \log \hat{\varepsilon} \\ \log \hat{q} \end{bmatrix} = \begin{bmatrix} \log(\widehat{q\hat{\varepsilon}^2}) \\ \log(\widehat{q\hat{\varepsilon}}) \\ \log(\widehat{\hat{\varepsilon}}) \end{bmatrix} \quad (58)$$

which we re-write into compact notation as

$$A_{eq} \overline{\log}(\hat{\theta}_{eq}) = \overline{\log}(\hat{\theta}_{pde}) \quad (59)$$

where  $\overline{\log}(\theta) = [\log(\theta_1), \log(\theta_2), \dots]^T$  is an element-wise operator. The parameter vector  $\hat{\theta}_{eq}$  can be uniquely solved from Eq. (58) via the Moore-Penrose pseudoinverse. Thus

$$\overline{\log}(\hat{\theta}_{eq}) = (A_{eq}^T A_{eq})^{-1} A_{eq}^T \overline{\log}(\hat{\theta}_{pde}) \quad (60)$$

This method works well in practice with respect to feeding parameter estimates into the adaptive observer (lower-left-hand block in Fig. 4), since the pseudoinverse ultimately involves computationally efficient matrix algebra.

## 5 Output Function Parameter Identification

The greatest difficulty in battery estimation arguably stems from the nonlinear relationship between SOC and voltage [9]. We directly address this difficulty by developing an identification algorithm for the uncertain parameters in the nonlinearly parameterized output function (9). First, we analyze parameter identifiability to assess which subset of parameters is uniquely identifiable. Second, we apply nonlinear least squares to this subset.

**5.1 Identifiability.** A necessary first step in nonlinear parameter identification is a parameter sensitivity analysis. We specifically apply the ranking procedure outlined in Ref. [27] to assess linear dependence. Consider the output function (9) written in parametric form:

$$\begin{aligned} h(t; \theta) = V(t) = & \frac{RT}{\alpha F} \sinh^{-1} \left[ \frac{\theta_2 I(t)}{2 \sqrt{c_{ss}^+(t; \theta_1) (c_{s,\max}^+ - c_{ss}^+(t; \theta_1))}} \right] \\ & - \frac{RT}{\alpha F} \sinh^{-1} \left[ \frac{\theta_3 I(t)}{2 \sqrt{c_{ss}^-(t) (c_{s,\max}^- - c_{ss}^-(t))}} \right] \\ & + U^+(c_{ss}^+(t; \theta_1)) - U^-(c_{ss}^-(t)) + \theta_4 I(t) \end{aligned} \quad (61)$$

where  $c_{ss}^+(t; \theta_1)$  and the parameter vector  $\theta$  are

$$\begin{aligned} c_{ss}^+(t; \theta_1) = & -\frac{\varepsilon_s^- L^-}{\varepsilon_s^+ L^+} c_{ss}^-(t) + \frac{\theta_1}{\varepsilon_s^+ L^+ A}, \\ \theta = & \left[ n_{Li}, \frac{1}{a^+ AL^+ k^+ \sqrt{c_e^0}}, \frac{1}{a^- AL^- k^- \sqrt{c_e^0}}, R_f \right]^T \end{aligned} \quad (62)$$

We have selected the elements of  $\theta$  because diminishing  $n_{Li}$  physically models capacity fade and increasing values for the other parameters capture various forms of internal resistance.

The following sensitivity analysis is performed in discrete time, since the required data is supplied in discrete time. Let  $k$  index time such that  $t = k\Delta T, k \in 1, 2, \dots, n_T$ . The sensitivity of the output with respect to variations in the parameter  $\theta_i$  at time index  $k$  is defined as  $S_{i,k} = \partial h(k\Delta T; \theta) / \partial \theta_i$ . For each parameter  $\theta_i$ , stack the sensitivities at time indices  $k = 1, 2, \dots, n_T$ , i.e.,  $S_i = [S_{i,1}, S_{i,2}, \dots, S_{i,n_T}]^T$ . Denote  $S = [S_1, S_2, S_3, S_4]$ , such that  $S \in R^{n_T \times 4}$ . A particular decomposition of  $S^T S$  reveals useful information about linear dependence between parameters. Let  $S^T S = D^T C D$  where

$$\begin{aligned} D = & \begin{bmatrix} \|S_1\| & 0 & 0 & 0 \\ 0 & \|S_2\| & 0 & 0 \\ 0 & 0 & \|S_3\| & 0 \\ 0 & 0 & 0 & \|S_4\| \end{bmatrix}, \\ C = & \begin{bmatrix} 1 & \frac{\langle S_1, S_2 \rangle}{\|S_1\| \|S_2\|} & \frac{\langle S_1, S_3 \rangle}{\|S_1\| \|S_3\|} & \frac{\langle S_1, S_4 \rangle}{\|S_1\| \|S_4\|} \\ \frac{\langle S_2, S_1 \rangle}{\|S_2\| \|S_1\|} & 1 & \frac{\langle S_2, S_3 \rangle}{\|S_2\| \|S_3\|} & \frac{\langle S_2, S_4 \rangle}{\|S_2\| \|S_4\|} \\ \frac{\langle S_3, S_1 \rangle}{\|S_3\| \|S_1\|} & \frac{\langle S_3, S_2 \rangle}{\|S_3\| \|S_2\|} & 1 & \frac{\langle S_3, S_4 \rangle}{\|S_3\| \|S_4\|} \\ \frac{\langle S_4, S_1 \rangle}{\|S_4\| \|S_1\|} & \frac{\langle S_4, S_2 \rangle}{\|S_4\| \|S_2\|} & \frac{\langle S_4, S_3 \rangle}{\|S_4\| \|S_3\|} & 1 \end{bmatrix} \end{aligned} \quad (63)$$

where  $\|\cdot\|$  denotes the Euclidian norm and  $\langle \cdot, \cdot \rangle$  is the inner product. By the Cauchy Schwarz inequality  $-1 \leq \langle \langle S_i, S_j \rangle / (\|S_i\| \|S_j\|) \rangle \leq 1$ . This has the interpretation that values of  $\langle \langle S_i, S_j \rangle / (\|S_i\| \|S_j\|) \rangle$  near  $-1$  or  $1$  imply strong linear dependence between parameters  $\theta_i$  and  $\theta_j$ , whereas values near zero imply orthogonality.

An example for the matrix  $C$  is provided in Eq. (64). This example analyzes parameter sensitivity for a UDDS drive cycle data set applied to the SPM battery model.

$$C = \begin{bmatrix} 1 & -0.3000 & 0.2908 & 0.2956 \\ -0.3000 & 1 & -0.9801 & -0.9805 \\ 0.2908 & -0.9801 & 1 & 0.9322 \\ 0.2956 & -0.9805 & 0.9322 & 1 \end{bmatrix} \quad (64)$$

Note that strong linear dependence exists between  $\theta_2, \theta_3, \theta_4$ . This property is uniformly true across various drive cycles (e.g., US06, SC04, LA92, and naturalistic microtrips). This means it is difficult to determine how each individual parameter value changes, amongst these three parameters. As a result, we identify only two parameters,  $n_{Li}$  and  $R_f$ .

*Remark 4.* Coincidentally, the parameters  $n_{Li}$  and  $R_f$  represent capacity and power fade, respectively. Identification of  $n_{Li}$  and  $R_f$  provides a direct system-level measurement of SOH—a particularly beneficial feature of this design.

*Remark 5.* Indeed, the matrix  $S^T S$  has an important interpretation in statistical mathematics—the inverse of the Fisher information matrix. From this interpretation, one may use the Cramer Rao lower bound to compute the individual variance contribution of each parameter [27].

**5.2 Nonlinear Least Squares.** Now our immediate goal is to identify the parameter vector  $\theta_h = [n_{Li} \ R_f]^T$  via a nonlinear least squares identification algorithm. Define  $\tilde{\theta}_h = \theta_h - \hat{\theta}_h$  and write Eq. (61) in terms of  $\tilde{\theta}_h$

$$V(t; \theta_h) = \frac{RT}{\alpha F} \sinh^{-1} \left[ \frac{I(t)}{2a^+ AL + i_0^+ (c_{ss}^+(t; \tilde{\theta}_{h1} + \hat{\theta}_{h1}))} \right] - \frac{RT}{\alpha F} \sinh^{-1} \left[ \frac{I(t)}{2a^- AL - i_0^- (c_{ss}^-(t))} \right] + U^+(c_{ss}^+(t; \tilde{\theta}_{h1} + \hat{\theta}_{h1})) - U^-(c_{ss}^-(t)) + (\tilde{\theta}_{h2} + \hat{\theta}_{h2})I(t) \quad (65)$$

Next, we take the Maclaurin series expansion with respect to  $\tilde{\theta}_h$

$$V(t; \theta_h) = \frac{RT}{\alpha F} \sinh^{-1} \left[ \frac{I(t)}{2a^+ AL + i_0^+ (c_{ss}^+(t; \hat{\theta}_{h1}))} \right] - \frac{RT}{\alpha F} \sinh^{-1} \left[ \frac{I(t)}{2a^- AL - i_0^- (c_{ss}^-(t))} \right] + U^+(c_{ss}^+(t; \hat{\theta}_{h1})) - U^-(c_{ss}^-(t)) + \hat{\theta}_{h2} I(t) + \frac{\partial h}{\partial \theta_{h1}}(t; \hat{\theta}_h) \tilde{\theta}_{h1} + I(t) \tilde{\theta}_{h2} + O(\tilde{\theta}_h^T \tilde{\theta}_h) \quad (66)$$

Truncate the higher order terms and re-arrange the previous expression into the matrix form

$$e_{nl} = \tilde{\theta}_h^T \Phi \quad (67)$$

where the nonlinear error term  $e_{nl}$  depends on the parameter estimates  $\hat{\theta}_h$  as

$$e_{nl} = V(t) - \frac{RT}{\alpha F} \sinh^{-1} \left[ \frac{I(t)}{2a^+ AL + i_0^+ (c_{ss}^+(t; \hat{\theta}_{h1}))} \right] + \frac{RT}{\alpha F} \sinh^{-1} \left[ \frac{I(t)}{2a^- AL - i_0^- (c_{ss}^-(t))} \right] - U^+(c_{ss}^+(t; \hat{\theta}_{h1})) + U^-(c_{ss}^-(t)) - \hat{\theta}_{h2} I(t) \quad (68)$$

and the regressor vector  $\Phi$  is defined as

$$\Phi = \left[ \frac{\partial h}{\partial \theta_{h1}}(t; \hat{\theta}_h), \ I(t) \right]^T \quad (69)$$

The vector  $\Phi$  in Eq. (69) depends upon measured signals and parameter estimates.

We now choose a least-squares parameter update law

$$\dot{\hat{\theta}}_h = P_h e_{nl} \Phi \quad (70)$$

$$\dot{P}_h = -P_h \frac{\Phi \Phi^T}{m_h^2} P_h, \quad P_h(0) = P_{h0} = P_{h0}^T > 0 \quad (71)$$

$$m_h^2 = 1 + \gamma_h \Phi^T \Phi, \quad \gamma_h > 0 \quad (72)$$

## 6 Adaptive Output Function Inversion

In Sec. 3, we designed a linear state observer using boundary values of the PDE. These boundary values must be processed from measurements by inverting the nonlinear output function. In this section, we design an adaptive output function inversion scheme which utilizes the parameter estimate  $\theta_h$  generated from Sec. 5.

Our goal is to solve  $g(c_{ss}^-, t) = 0$  for  $c_{ss}^-$ , where

$$g(c_{ss}^-, t) = \frac{RT}{\alpha F} \sinh^{-1} \left[ \frac{I(t)}{2a^+ AL + i_0^+ (c_{ss}^+(t; \hat{\theta}_{h1}))} \right] - \frac{RT}{\alpha F} \sinh^{-1} \left[ \frac{I(t)}{2a^- AL - i_0^- (c_{ss}^-(t))} \right] + U^+(c_{ss}^+(t; \hat{\theta}_{h1})) - U^-(c_{ss}^-(t)) + \hat{\theta}_{h2} I(t) - V(t) \quad (73)$$

The main idea is to construct an ODE whose equilibrium satisfies  $g(c_{ss}^-, t) = 0$  and is locally exponentially stable. This can be viewed as a continuous-time version of Newton's method for solving nonlinear equations [25]. Consider the ODE

$$\frac{d}{dt} [g(\tilde{c}_{ss}^-, t)] = -\gamma g(\tilde{c}_{ss}^-, t) \quad (74)$$

whose equilibrium satisfies  $g(c_{ss}^-, t) = 0$ . We expand and re-arrange this equation into the familiar Newton's update law

$$\frac{d}{dt} \tilde{c}_{ss}^- = - \left[ \frac{\partial g}{\partial c_{ss}^-}(\tilde{c}_{ss}^-, t) \right]^{-1} \left[ \gamma g(\tilde{c}_{ss}^-, t) + \frac{\partial g}{\partial t}(\tilde{c}_{ss}^-, t) \right] \quad (75)$$

One can prove Lyapunov stability of this ODE, given appropriate bounds  $\partial g / \partial c_{ss}^-$  and  $\partial g / \partial t$ . The bounds on  $\partial g / \partial c_{ss}^-$  use the strictly decreasing property of  $U^+(\cdot)$  and  $U^-(\cdot)$  in Eq. (73). The state  $\tilde{c}_{ss}^-$  of ODE (75) provides a recursive estimate of the surface concentration  $c_{ss}^-(t)$  from measured current and voltage data, adapted according to the parameter estimate  $\hat{\theta}_h$ . The processed surface concentration  $\tilde{c}_{ss}^-$  supplies the "measured output" for the state estimator in Sec. 3.

In practice, it is undesirable to compute derivatives of measured data  $I(t)$  and  $V(t)$  to calculate  $\partial g / \partial t$  in Eq. (75). Therefore, we use the same filtering concept employed in the PDE parameter identifier in Sec. 4.2 to avoid differentiation.

## 7 Simulations

In this section, we present numerical experimental results, which demonstrate the adaptive PDE observer's performance. Specifically, we apply the observer to the full order DFN model. The model parameters used in this study originate from the publicly available DUALFOIL simulation package [18].

For all simulations, the state and parameter estimates are initialized at incorrect values:  $\hat{c}_s^-(r, 0) = \frac{1}{2} c_s^-(r, 0)$ ,  $\hat{\varepsilon}(0) = 2$ ,  $\hat{q} = 0.5$ ,  $\hat{n}_{Li}(0) = 1.25 n_{Li}$ ,  $\hat{R}_f(0) = 3 R_f$ . Moreover, zero mean normally distributed noise with a standard deviation of 10 mV is added to the voltage measurement.

**7.1 Electric Vehicle Charge/Discharge Cycle.** First, we apply an electric vehicle-like charge/discharge cycle. This input signal is generated from two concatenated UDDS drive cycles simulated on the models developed in Ref. [28]. This signal is a highly transient input with large magnitude C-rates, thereby producing a sufficiently rich signal for parameter estimation. Figure 6 portrays the evolution of the state and parameter estimates. The state estimates are represented by the bulk SOC, defined in Eq. (76), and surface concentrations.

$$\widehat{\text{SOC}}(t) = \frac{3}{c_{s,\max}^-} \int_0^1 r^2 \hat{c}_s^-(r, t) dr \quad (76)$$

The PDE parameter estimates  $\hat{\varepsilon}$ ,  $\hat{q}$  and output function parameter estimates  $\hat{n}_{Li}$ ,  $\hat{R}_f$ , which are normalized to one in Fig. 6, also converge near their true values. Indeed, one expects some estimation bias for such a nonlinear and complex model. An expected estimation bias exists in  $\hat{\varepsilon}$  and  $\hat{q}$  due to the overparameterization of the



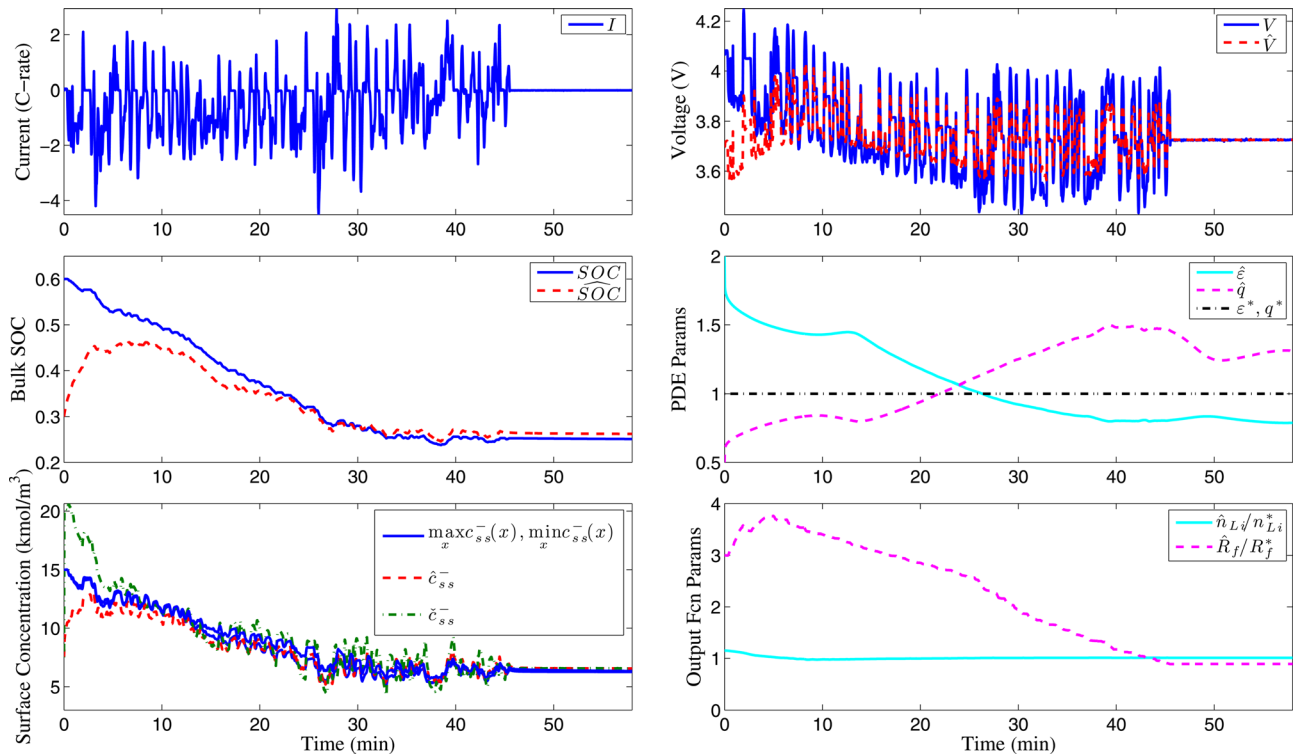


**Fig. 6** Evolution of state and parameter estimates for UDDSx2 charge/discharge cycle. Zero mean Gaussian noise with a 10 mV variance was added to the voltage measurement. The DFN model provides the “measured” plant data. State and parameter estimates were initialized with incorrect values.

Padé approximation. The nonlinear least squares method for  $\hat{n}_{Li}$  and  $\hat{R}_f$  will also generally produce bias. To mitigate bias, one needs to carefully select the adaptation gains, as discussed in Sec. 8. Similar results are achievable for various other initial conditions and drive cycle inputs, including US06, SC04, LA92, and naturalistic microtrip data.

**7.2 Constant 1C Discharge Cycle.** Next, we apply a constant 1C discharge for 20 min, followed by a 10 min relaxation period. Figure 7 portrays the evolution of the state and parameter estimates. Since the SPM does not predict polarization effects due to the electrolyte, the state estimates are biased during discharge, as a consequence of driving the voltage error to zero. During relaxation, however, the state estimate recovers since the SPM and DFN model become identical at equilibrium. This result is a direct consequence of using the SPM. In spite of an input that lacks sufficient richness, the PDE parameters converge near the true values. However, one may numerically check that the persistency of excitation level for the output parameters is not sufficiently high enough to produce convergent estimates. This demonstrates that an ideal input signal does not contain sustained high C-rates and is sufficiently rich.

**7.3 No Parameter Adaptation.** Next, we examine the impact of setting the parameter adaptation gains to zero. This scenario examines the utilization of a state estimator with uncertain parameters. Figure 8 presents the evolution of the state estimates for an EV-like charge/discharge cycle. Note the bulk SOC and surface concentrations exhibit large bias, even during relaxation. This bias is mainly attributed to the 15% error in the parameter  $n_{Li}$ . Consequently, we conclude that accurate knowledge of the model parameters and/or online adaptation is crucial for accurate state estimates.

*Remark 6.* Experimental validation of the state and parameter estimates is difficult. An open challenge in battery systems

and control is in situ measurements of lithium concentration, diffusion coefficients, cyclable lithium, SEI resistive layers, etc. Some recent progressions include neutron imaging [3], electrochemical strain microscopy [29], and three electrode cells [30].

## 8 Gain Selection

Due to the bi-directionally coupled relationship between the state and parameter estimates, gain selection is a highly nontrivial task. However, we have developed a systematic procedure for tuning these gains.

The most important gains are summarized in Table 2, along with their design criteria. The parameter  $\lambda$  translates the spectrum of the target system (24)–(26) along the real-axis. The matrix  $P_{pde0}$  supplies the initial condition for the covariance matrix in the PDE parameter least squares estimator. We select  $P_{pde0} = \rho_{pde} I$ , where  $\rho_{pde}$  is the tuning gain. The matrix  $P_{h0}$  supplies the initial condition for the covariance matrix in the output function parameter least squares estimator. We select  $P_{h0} = \text{diag}(P_{h011}, P_{h022})$ , where  $P_{h011}, P_{h022}$  are the tuning gains. To begin, set all gains to zero. The tuning procedure is as follows:

**Step 1: Fix  $\lambda$ .**—This provides the desired convergence rate for the state  $c(r, t)$ .

**Step 2: Design  $P_{h011}$ .**—The parameter  $n_{Li}$  and state  $c(r, t)$  are intimately related, due to the relation in Eq. (8). In particular, these two estimates must converge at similar rates. If they converge at dissimilar rates, the estimates produce bias in each other. Examples are provided in Fig. 9.

**Step 3: Design  $P_{h022}$ .**—Progressively increase  $P_{h022}$  until the desired convergence rate is obtained, without significantly impacting the convergence of  $c(r, t)$  and  $n_{Li}$ .

**Step 4: Design  $\rho_{pde}$ .**—Progressively increase  $\rho_{pde}$  until the desired convergence rate is obtained, without significantly impacting the other estimates.

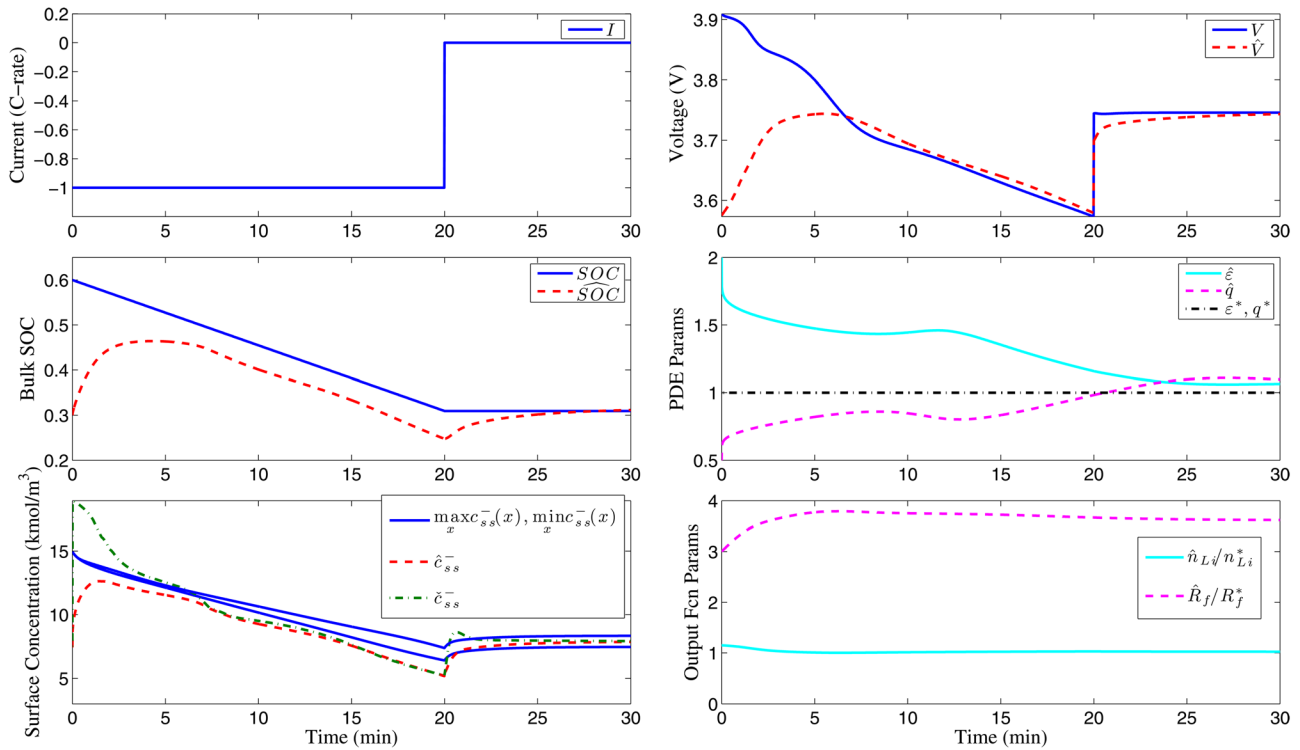


Fig. 7 Evolution of state and parameter estimates for a 20 min 1 C discharge and 10 min relaxation

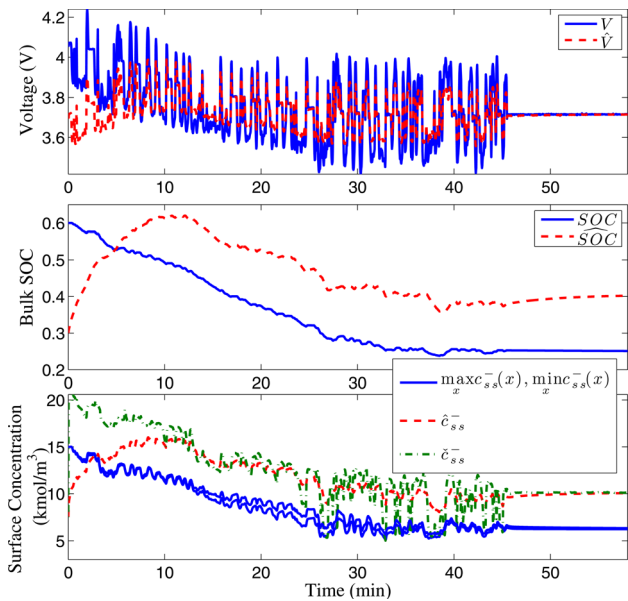


Fig. 8 Evolution of state estimates for UDDSx2 charge/discharge cycle with no parameter adaptation. Accurate parameter values and/or online adaptation are critical for unbiased estimates.

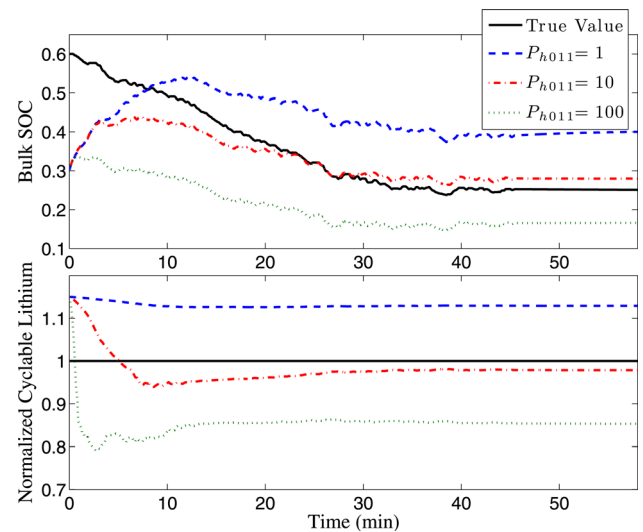


Fig. 9 Relationship between  $\hat{c}(r, t)$  (i.e.,  $\widehat{\text{SOC}}$ ) and  $\hat{n}_{\text{Li}}$ , for varying  $P_{h011}$  and  $\lambda = -1$ . An improper selection between these two gains results in biased estimates.

Table 2 Important adaptive observer gains

Gain	State/Parameter	Eqs.	Design criteria
$\lambda$	$\hat{c}(r, t)$	(37)–(39)	$\lambda < \varepsilon/4 < 0$
$P_{pde0}$	$\hat{\varepsilon}, \hat{q}$	(55)	$P_{pde0} = P_{pde0}^T > 0$
$P_{h0}$	$\hat{n}_{\text{Li}}, \hat{R}_f$	(71)	$P_{h0} = P_{h0}^T > 0$

## 9 Conclusion

This paper reports on the first combined SOC/SOH estimator for electrochemical battery models. The adaptive observer utilizes concepts from PDE estimation and adaptive control theory to generate various new concepts for battery systems and control. These are summarized by four key ideas: First, a backstepping PDE state estimator is designed in previous work [14]. Second, a Padé approximation of the transfer function for lithium diffusion is used to identify the diffusion coefficient. Third, parameter

sensitivity analysis is applied to elucidate the linear dependence between physically meaningful parameters related to capacity and power fade. Fourth, an adaptive output function inversion technique enables linear state estimation designs. Finally, we present simulations which demonstrate how the adaptive observer performs against a high-fidelity battery simulator—the Doyle-Fuller-Newman model. The composition of these unique ideas provides a combined SOC/SOH estimation algorithm for battery systems using electrochemical models.

A useful extension of the observer presented here is a state/parameter estimator for the DFN model. In particular, this would enable improved estimation accuracy at high C-rates. Moreover, the DFN model predicts additional SOH-critical variables, such as side reaction overpotentials. On-going work is also centered around output-feedback control schemes that utilize the presented observer to maximize energy/power while satisfying safe operating constraints.

## Nomenclature

$A$  = cell cross sectional area,  $m^2$   
 $a^j$  = specific interfacial surface area,  $m^2/m^3$   
 $c_e^0$  = Li concentration in electrolyte phase,  $mol/m^3$   
 $c_s^j$  = Li concentration in solid phase,  $mol/m^3$   
 $c_{ss}^j$  = Li concentration at particle surface,  $mol/m^3$   
 $c_{s,max}^j$  = max Li concentration in solid phase,  $mol/m^3$   
 $D_s^j$  = diffusion coefficient in solid phase,  $m^2/s$   
 $F$  = Faraday's constant,  $C/mol$   
 $I$  = input current,  $A$   
 $i_0^j$  = exchange current density,  $V$   
 $j$  = positive (+) or negative (−) electrode  
 $k^j$  = reaction rate,  $A \cdot mol^{1.5}/m^{5.5}$   
 $L^j$  = electrode thickness,  $m$   
 $n_{Li}$  = total number of Li ions,  $mol$   
 $q$  = boundary input coefficient parameter  
 $R$  = universal gas constant,  $J/mol-K$   
 $R_f$  = lumped current collector resistance,  $\Omega$   
 $R_s^j$  = particle radius,  $m$   
 $r$  = radial coordinate,  $m$ , or  $m/m$   
 $T$  = cell temperature,  $K$   
 $t$  = time,  $s$   
 $U^j$  = equilibrium potential,  $V$   
 $V$  = output voltage,  $V$   
 $\alpha^j$  = anodic/cathodic transfer coefficient  
 $\varepsilon$  = diffusion parameter  
 $\varepsilon_s^j$  = volume fraction of solid phase

## References

- [1] Chaturvedi, N. A., Klein, R., Christensen, J., Ahmed, J., and Kojic, A., 2010, "Algorithms for Advanced Battery-Management Systems," *IEEE Control Systems Magazine*, **30**(3), pp. 49–68.
- [2] Moura, S., Fathy, H., Callaway, D., and Stein, J., 2011, "A Stochastic Optimal Control Approach for Power Management in Plug-in Hybrid Electric Vehicles," *IEEE Trans. Control Syst. Technol.*, **19**(3), pp. 545–555.
- [3] Siegel, J. B., Lin, X., Stefanopoulou, A. G., Hussey, D. S., Jacobson, D. L., and Gorsich, D., 2011, "Neutron Imaging of Lithium Concentration in LFP Pouch Cell Battery," *J. Electrochem. Soc.*, **158**(5), pp. A523–A529.
- [4] Liu, P., Wang, J., Hicks-Garner, J., Sherman, E., Soukiazian, S., Verbrugge, M., Tataria, H., Musser, J., and Finamore, P., 2010, "Aging Mechanisms of LiFePO<sub>4</sub> Batteries Deduced by Electrochemical and Structural Analyses," *J. Electrochem. Soc.*, **157**(4), pp. A499–A507.

- [5] Thomas, K., Newman, J., and Darling, R., 2002, *Advances in Lithium-Ion Batteries*, Mathematical Modeling of Lithium Batteries, Kluwer Academic/Plenum Publishers, New York, Chap. XII, pp. 345–392.
- [6] Plett, G. L., 2004, "Extended Kalman Filtering for Battery Management Systems of LiPB-Based HEV Battery Packs. Part 3. State and Parameter Estimation," *J. Power Sources*, **134**(2), pp. 277–292.
- [7] Verbrugge, M., and Tate, E., 2004, "Adaptive State of Charge Algorithm for Nickel Metal Hydride Batteries Including Hysteresis Phenomena," *J. Power Sources*, **126**(1–2), pp. 236–249.
- [8] Verbrugge, M., 2007, "Adaptive, Multi-Parameter Battery State Estimator With Optimized Time-Weighting Factors," *J. Appl. Electrochem.*, **37**(5), pp. 605–616.
- [9] Hu, Y., and Yurkovich, S., 2012, "Battery Cell State-of-Charge Estimation Using Linear Parameter Varying System Techniques," *J. Power Sources*, **198**, pp. 338–350.
- [10] Santhanagopalan, S., and White, R. E., 2006, "Online Estimation of the State of Charge of a Lithium Ion Cell," *J. Power Sources*, **161**(2), pp. 1346–1355.
- [11] Domenico, D. D., Stefanopoulou, A., and Fiengo, G., 2010, "Lithium-Ion Battery State of Charge and Critical Surface Charge Estimation Using an Electrochemical Model-Based Extended Kalman Filter," *ASME J. Dyn. Syst., Meas., Control*, **132**(6), p. 061302.
- [12] Smith, K. A., Rahn, C. D., and Wang, C.-Y., 2008, "Model-Based Electrochemical Estimation of Lithium-Ion Batteries," 2008 IEEE International Conference on Control Applications, pp. 714–719.
- [13] Klein, R., Chaturvedi, N. A., Christensen, J., Ahmed, J., Findeisen, R., and Kojic, A., 2012, "Electrochemical Model Based Observer Design for a Lithium-Ion Battery," *IEEE Trans. Control Syst. Technol.*, pp. 1–13.
- [14] Moura, S. J., Chaturvedi, N., and Krstic, M., 2012, "PDE Estimation Techniques for Advanced Battery Management Systems—Part I: SOC Estimation," *Proceedings of the 2012 American Control Conference*.
- [15] Moura, S. J., Chaturvedi, N., and Krstic, M., 2012, "PDE Estimation Techniques for Advanced Battery Management Systems—Part II: SOH Identification," *Proceedings of the 2012 American Control Conference*.
- [16] Moura, S. J., Chaturvedi, N., and Krstic, M., 2012, "Adaptive PDE Observer for Battery SOC/SOH Estimation," 2012 ASME Dynamic Systems and Control Conference.
- [17] Santhanagopalan, S., Guo, Q., Ramadass, P., and White, R. E., 2006, "Review of Models for Predicting the Cycling Performance of Lithium Ion Batteries," *J. Power Sources*, **156**(2), pp. 620–628.
- [18] Newman, J., 2008, Fortran Programs for the Simulation of Electrochemical Systems, University of California, Berkeley, CA.
- [19] Chen, C., 1998, *Linear System Theory and Design*, Oxford University Press, Inc., Oxford, UK.
- [20] Krstic, M., and Smyshlyayev, A., 2008, *Boundary Control of PDEs: A Course on Backstepping Designs*, Society for Industrial and Applied Mathematics, Philadelphia, PA.
- [21] Delacourt, C., Poizat, P., Levasseur, S., and Masquelier, C., 2006, "Size Effects on Carbon-Free LiFePO<sub>4</sub> Powders," *Electrochem. Solid-State Lett.*, **9**(7), pp. A352–A355.
- [22] Derrien, G., Hassoun, J., Panero, S., and Scrosati, B., 2007, "Nanostructured Sn-C Composite as an Advanced Anode Material in High-Performance Lithium-Ion Batteries," *Adv. Mater.*, **19**(17), pp. 2336–2340.
- [23] Forman, J. C., Moura, S. J., Stein, J. L., and Fathy, H. K., 2012, "Genetic Identification and Fisher Identifiability Analysis of the Doyle-Fuller-Newman Model From Experimental Cycling of a LiFePO<sub>4</sub> Cells," *J. Power*, **210**, pp. 263–275.
- [24] Khalil, H. K., 2002, *Nonlinear Systems*, 3rd ed., Prentice Hall, Englewood Cliffs, NJ.
- [25] Ioannou, P., and Sun, J., 1996, *Robust Adaptive Control*, Prentice-Hall, Englewood Cliffs, NJ.
- [26] Smyshlyayev, A., and Krstic, M., 2010, *Adaptive Control of Parabolic PDEs*, Princeton University, Princeton, NJ.
- [27] Lund, B. F., and Foss, B. A., 2008, "Parameter Ranking by Orthogonalization—Applied to Nonlinear Mechanistic Models," *Automatica*, **44**(1), pp. 278–281.
- [28] Moura, S. J., Stein, J. L., and Fathy, H. K., 2012, "Battery-Health Conscious Power Management in Plug-In Hybrid Electric Vehicles Via Electrochemical Modeling and Stochastic Control," *IEEE Trans. Control Syst. Technol.*, **21**, pp. 679–694.
- [29] Morozovska, A., Eliseev, E., Balke, N., and Kalinin, S., 2010, "Local Probing of Ionic Diffusion by Electrochemical Strain Microscopy: Spatial Resolution and Signal Formation Mechanisms," *J. Appl. Phys.*, **108**(5), p. 053712.
- [30] Fang, W., Kwon, O. J., and Wang, C.-Y., 2010, "Electrochemical-Thermal Modeling of Automotive Li-Ion Batteries and Experimental Validation Using a Three-Electrode Cell," *Int. J. Energy Res.*, **34**(2), pp. 107–115.